Book of Tutorials and Abstracts

European Microbeam
Analysis Society

EMAS 2026

15th
REGIONAL WORKSHOP

TOPICAL CONFERENCE ON ELECTRON BACKSCATTER DIFFRACTION (EBSD)

14 to 17 June 2026
at the
CentraleSupélec, Gif-sur-Yvette, France

Organised in collaboration with:
ICMMO, ENS Paris-Saclay,
Université Paris-Saclay

EMAS
European Microbeam Analysis Society eV
www.microbeamanalysis.eu/

This volume is published by:
European Microbeam Analysis Society eV (EMAS)
EMAS Secretariat
c/o Eidgenössische Technische Hochschule, Department of Earth and Planetary Sciences
Clausiusstrasse 25
8092 Zürich
Switzerland

ISBN 978 90 8227 6992
NUR code: 971 – Materials Science

3D ORIENTATION MICROSCOPY (3D-EBSD)

Peter J. Konijnenberg*, S. Zaefferer and D. Raabe

Max-Planck Institute for Sustainable Materials, Diffraction and Microscopy Group
Max-Planck Strasse 1, 40237 Düsseldorf, Germany
e-mail: p.konijnenberg@mpi-susmat.de

Peter Konijnenberg earned his degree in materials science from RWTH Aachen University in 1999, after which he stayed there as a researcher at the Institute for Physical Metallurgy and Materials Physics. In 2006, he moved to Denmark to take up a position as a software scientist at Oxford Instruments-HKL Technology, where his work included research on EBSD and EDS, EBSD at elevated temperatures, 3D-EBSD and EBSD on out-of-plane structures. In 2010, he joined the Max Planck Institute for Sustainable Materials (formerly MPIE) in Düsseldorf to focus on 3D-EBSD for a wide range of materials. During this time, he served as the principal developer of the QUBE software package and made significant contributions to the development of an automated 3D-EBSD system, ELAVO 3D. In 2014, he joined Bruker Nano in Berlin, while seconded to the Max Planck Institute, to commercialise the QUBE software package. In 2021, he became a member of the Institute for Advanced Simulation at the Jülich Research Center, concentrating on materials informatics with a focus on electron microscopy and diffraction. Since 2025, he is again affiliated with the Max Planck Institute for Sustainable Materials. He has (co-)authored over 50 publications and book chapters and has presented his work at international conferences worldwide. His research interests span from electron microscopy and diffraction to materials informatics and experimental hardware development, as well as from structural to geological and functional materials.

1. ABSTRACT

We present a brief overview of some selected aspects of 3D-EBSD. Currently available techniques for serial sectioning in the field of 3D-EBSD are compared regarding their capabilities and potentials. Furthermore, challenges and opportunities in the area of data set reconstruction and 3D description of boundaries are discussed. Finally, we identify and discuss problem classes for which 3D-EBSD provides a suitable solution.

2. INTRODUCTION

Microstructures are usually characterised by statistical measures derived from 2D cross-sectional data. Nevertheless, in cases where 3D statistics matter, orthogonal cross-sections or stereological methods merely deliver approximate distributions. When a higher accuracy is needed or when the direct relation of structure and properties is necessary (e.g., the correlation of corrosion behaviour with grain boundary character), a truly 3D representation is indispensable via tomographic methods. Of particular interest are those tomographic techniques that allow a detailed microstructure analysis. This includes the morphological, chemical and crystallographic description of crystals and of grain and phase boundaries, the characterisation of precipitates as well as the quantification of dislocations or other crystallographic defects. Furthermore, the morphology and crystallography of cracks or other internal surfaces may be relevant.

Destructive tomography combined with analytical scanning electron microscopy, is evolving into a technique capable of analysing increasingly vast volumes at high spatial and angular resolutions. The present work focusses on 3D-electron backscatter diffraction (3D-EBSD), some of its concepts, issues and challenges as well as highlighting some suitable applications.

3. TOMOGRAPHY

Generally, in materials science, every technique that displays and quantifies a 3D object from a bulk material is addressed as tomography. This includes destructive techniques that actually cut an object into thin slices like ultra-microtomy for biological samples [1], techniques that remove thin layers from the surface of a bulk material, e.g., by mechanical polishing [2, 3], focussed ion beam (FIB) cutting [4, 5], broad ion beam sputtering [6, 7], or laser ablation [8], and techniques that observe the 3D structure of a material non-destructively by some sort of transmissive radiation, e.g., ultrasound [9], X-rays [10, 11] or electrons [12].

For tomography by serial sectioning one of the most suitable observation techniques is electron backscatter diffraction (EBSD) in the scanning electron microscope (SEM) because it has reached a very high degree of automation and allows a comprehensive description of microstructures with high spatial (~ 50 nm) and angular (~ 0.1°) resolution. In combination with energy-dispersive X-ray spectrometry (EDS) it allows the measurement of elemental composition with reasonably good accuracy (~ 1 at% at 100 nm resolution). Both EBSD and EDS are relatively slow scanning techniques with measurement times per dwell point between 1 to 100 ms or even seconds for EDS. Because both techniques become less accurate when scanning speed is increased one needs to find compromises between measurement time and accuracy. Often EBSD or EDS maps for tomographic techniques take between 10 minutes and 1 hour and are, therefore, the temporal bottleneck for the techniques where several hundred serial sections are to be characterised which finally may take several days or even weeks of acquisition time.

In the following we will introduce some of the destructive, serial sectioning techniques that allow comprehensive investigation of microstructures of crystalline matter in some more detail.

3.1. Serial block face SEM (SBFSEM)

Thin slices of material are cut from a surface of a free standing pillar using a sharp diamond knife mounted inside of an SEM. The remaining surface is observed by SEM-based techniques, including EBSD. The samples need to be small with a cross-section of about 500 × 500 μm^2. The slices can be as thin as 15 nm to 50 nm, and areas as large as approx. 200 × 200 μm^2 can be imaged. Slice thickness is controlled by electronic sample feed. The cutting per slice takes only about 1 s. SBFSEM is mainly used to slice biological samples, either in a hard resin or under cryogenic conditions [13, 14], but it has also been employed to cut metals, like Al or Mg alloys and steels and, despite some shear damage, EBSD patterns are obtained from the surface [15]. Nevertheless, it appears that the technique is not generally suited for microstructure analysis of hard matter.

3.2. Chemo-mechanical polishing using a robotic system

Thin layers of material are polished off from a specimen mounted for metallographic preparation using a fully automated versatile polishing automaton outside of the SEM [2, 3, 16]. The automaton also cares for cleaning and drying the sample. Next, the sample is automatically transferred to the SEM using a co-operative robot that places the sample into a dedicated sample holder in the SEM. After evacuating the SEM chamber and automatically positioning the sample, SEM-based observations are performed. Finally, the sample is returned to the polishing robot for the next polishing step. The automated preparation, which includes a final chemo-mechanical polishing step, results in large (up to cm^2), artefact-free and perfectly flat sample surfaces, ideally suited for EBSD, backscatter electron (BSE) or EDS observations and for further experiments, e.g., corrosion tests, deformation tests or, thermal treatment. This, together with the large 3D-investigated volume of up to 1 mm^3, is a very important aspect of the technique as it allows the correlation of macroscopic properties, e.g., corrosion rates, with 3D microscopic features, e.g., 5-parameter grain boundary character. The currently smallest slice thickness is 0.5 µm. The accurate measurement and control of slice thickness is still a matter of development. Slice removal takes about 15 minutes including cleaning and drying, which results in a shortest possible cycle time of about 40 minutes, including measurement of a large EBSD/EDS map. Every material that can be prepared for EBSD or EDS mapping by metallographic techniques can be investigated. Samples sensitive to air or polishing liquids (e.g., lithium or sodium in battery materials) cannot be handled. The technique is particularly suited to obtain good statistics on grain boundary behaviour or grain morphology of materials with crystallite sizes of 20 µm and larger. One of the most important shortcomings of the technique is the necessity to transfer the sample into and out of the SEM, which creates positional inaccuracies and requires time.

3.3. Serial sectioning by a focussed ion beam (FIB)

A sample is placed in a dual beam FIB-SEM instrument and a thin layer of material is removed using ion-beam sputtering (“milling”) in grazing incidence starting from a sample edge [4, 17] or on a freely standing micro-pillar [18]. Ions are usually Ga^+ or Xe^+ in a plasma-FIB (PFIB), usually accelerated to 30 kV. After milling the sample is moved to the position for EBSD/EDS observation, which involves a significant sample tilt or rotation. After EBSD mapping the sample is returned to the milling position and the process is repeated. The thinnest slice that can be reliably and repeatedly removed is in the order of 50 nm and the maximum volumes that can be investigated are between $20 \times 20 \times 20\ \mu m^3$ for a Ga-FIB [2, 4] and $200 \times 200 \times 200\ \mu m^3$ for a PFIB [19]. These are suitable values for materials with crystallite sizes in the order of 5 to 20 µm. For materials with larger grain sizes, statistics of grain boundaries or grain morphology become poor. Milling one slice takes between 10 and 15 minutes, resulting in a total cycle time of 30 to 40 minutes including EBSD/EDS mapping. Most (P)FIB investigations have been performed on metallic samples because metals suffer less than other materials from amorphisation by the ion beam. Generally, a Ga^+-beam leads to larger crystallographic damage than Xe^+-beam. Finally, due to the special shape of the sampled material (pillars or trenches) these volumes are usually not easily accessible for further investigations.

3.4. Serial sectioning by coupled PFIB and femto-second laser

To allow investigations of very large volumes the PFIB has been coupled with a femto-second laser [8, 20] in a single instrument. A thin layer of material (thickness in the order of 1 µm) is removed by a femto-second laser with beam size of < 5 µm, directed in grazing incidence to the sample surface. For a $1 \times 1\ mm^2$ large area this may take a few minutes. The material is removed by an ablation process in which the electrons of the material are heated very significantly, leading to the formation of a plasma. This process creates relatively little damage or modification to the remaining material such that hard materials (like superalloys) can be directly observed by EBSD, while more sensitive materials, e.g., Ti-alloys, require a refinement with a PFIB ion beam, which adds further minutes to the sectioning process. During laser ablation a large amount of material is released from the sample, which subsequently deposits in the area around the ablation process.

To avoid contamination of the SEM, the sample is either shielded during the ablation process or it is moved into a separate chamber. With a laser-FIB system samples of a CoNi superalloy as large as 1 mm^3 have been investigated by EBSD with a voxel step size of 1.5 µm.

3.5. Serial sectioning by broad ion beam (BIB)

A thin layer of material is sputtered off from a sample surface using a broad Ar^+-ion beam arriving at the sample in grazing incidence [7]. A sharp cut is achieved using a protective shield made of an ion-resistant material (Ti or Mo) in front of the sample. In the most current version of the technique the BIB instrument is vacuum-connected to an SEM and the sample is transferred between both instruments by a mechanical transfer system. The BIB sputters areas up to several millimetres in diameter but the most typical observation area has a diameter of one millimetre inside which the area remains very flat with only a few microns of height variation. In contrast, the ion beam may lead to the formation of significant local sputtering craters at places of different hardness, e.g., hard precipitates or differently hard orientations. The quality of the crystal lattice remains higher than during Ga^+- or Xe^+-ion sputtering, leading to high quality EBSD maps on many different materials [6]. The sputtered layer thickness can be varied between ~10 nm and 1 µm. The sputtering of one layer on metals takes usually in the order of 10 minutes, resulting, like the other 3D techniques, in total cycle times of 30 to 45 minutes. The largest volume that has been reported being analysed by BIB-EBSD/EDS is in the order of $200 \times 200 \times 50$ μm^3, though it could be larger in principle.

3.6. Sub conclusion

Comparing all mentioned serial sectioning microstructure techniques, the BIB technique appears to be the most powerful and versatile as it can handle very different materials, including air-sensitive ones, very large volumes and very high resolution (< 100 nm) measurements. Also, the milling time is short and surfaces of high crystal quality are created. The laser-FIB technique may allow measurements of larger volumes but the resolution is limited to about 1 µm. The chemo-mechanical polishing technique creates very large surfaces with best surface and crystal quality. This makes it ideally suited e.g., for the measurement of large numbers of grain boundaries close to the surface and subsequent property measurements. The technique is, however, limited to materials that are insensitive to air and polishing liquids. For all techniques the EBSD/EDS mapping takes about the same time as the sectioning. Total cycle times range, for all techniques between 30 minutes and 1 hour for typical investigation sizes.

4. SLICE REGISTRATION

4.1. Errors and transformations

In destructive tomography, an integral 3D data set is compiled from multiple individual 2D data sets (slices), during a post-processing step. The consistency of the 3D stack tends to rely strongly on the slice registration. In this procedure neighbouring slices are brought into agreement with one another, such that various microstructural constituents are reconstructed in the 3rd dimension with minimal serrations.

In case of missing or deteriorated slices machine learning approaches have been developed to recover such slices, see e.g., [21, 22]. Usually, however, mismatch errors between neighbouring slices need to be corrected. The errors occurring during data acquisition vary in type and origin. The specimen handling and sectioning primarily introduces errors, such as shifts, rotations, non-parallelism or non-planarity. In contrast, the sampling of the specimen surface is predominantly affected by typical acquisition errors, such as scan field distortions caused by drift or specimen tilt.

Many of the 2D in-plane errors can be described as affine transformations, comprising combinations of rotation, scaling, shearing and translations. These errors can be readily corrected for, via a uniform back-transformation that is determined through a comparison with neighbouring slices or reference images obtained with another imaging modality.

Non-affine scan field distortions present a far greater challenge. Frequently, these distortions are subtle enough to remain unperceived in 2D, but still serious enough to deteriorate the microstructure consistency in the 3rd dimension. Their primary origin lies in electrostatic or thermal drift phenomena, which distort the raster scan field during acquisition. A correction of these distortions is computationally more expensive.

In an ideal case, a registration reference is collected for every slice. Preferably, this reference is acquired at zero tilt, to minimise adverse effects from foreshortening [23] and sufficiently fast, to minimise effects from drift, e.g., with a BSE detector or even optical means. A challenge lies in the different contrasts of EBSD and e.g., BSE maps. Via multimodal approaches slices can be registered to their respective references, see e.g., [24-26].

Data sets without specific reference images require different registration approaches. One is to identify the least drifted slice, e.g., the first slice or a slice in the middle, from which a pairwise registration is propagated throughout the entire stack. An objective function for the registration process can be e.g., a maximisation of the cross-correlation or a minimisation of the average misorientation angle between slices [27]. This approach tends to stack dominant microstructural features on top of each other. Hence, a balanced set of spatially differently oriented microstructural features needs to be selected. A powerful algorithm for non-rigid registration is the Smart-align algorithm that will be described in more detail in the following.

4.2. Smart-align

Non-rigid registration of images is well established in many areas of science involved with image analysis. Smart-align has been successfully applied for image-enhancement in the STEM field [28]. Based on classical image analysis, it calculates a displacement field to register two subtly different images, based on the gradients present in both images. A further key feature of Smart-align is that it utilises the raster-scan wise data collection of microscopy images. Both characteristics make it applicable to tomographic stacks, obtained by SEM techniques, such as EBSD and EDS.

The algorithm is derived from a modified optical flow equation (a.k.a. the brightness change constraint equation), which describes the displacement of objects from two slightly different images taken before and after the displacement. The equation solves a displacement field and is underdetermined but becomes solvable via regularisation. For this, two constraints are introduced, a similarity constraint which demands that the displacement is minimised and a global smoothness constraint to the displacement field, to ensure that it varies only gradually and is interpolated in regions with low gradient. The displacement field is solved iteratively by adding after each cycle the current displacement field to a cumulative displacement field. The latter is then applied to the second image to bring it gradually more into agreement with the first image. This process is repeated until some stopping criterion is reached.

Since drift varies (often erratically) with time, its effects show least for scan field points that were captured in rapid succession, such as neighbouring points within the same scan line. Hence, for EBSD or EDS maps a scan line represents an entity, which might be positioned wrong due to drift but which in itself is still largely correct. This is reflected by the “row/column lock” concept by which the displacement of entire scan lines is averaged [28]. For a tomographic stack this concept also provides some tolerance towards variations between neighbouring slices.

Since the Smart-align method operates with the image gradient, orientation maps must be first dimensionally reduced to grey-scale images. Once a displacement field is determined, it can be applied again to the original orientation map. For this, interpolations between individual orientations are necessary, which are only meaningful for similar orientations of the same phase. We use an adapted weighted bilinear approach.

Furthermore, some attention must be paid to steep gradients at high angle grain boundaries. It is essential to stretch these gradients in the grey-scale images, e.g., by a moderate Gaussian smoothing, to ensure some essential overlap between features in both images. However, this comes at the cost of some loss in spatial resolution.

As an example, in Fig. 1 a 3D EBSD data set is shown that was acquired with our ELAVO 3D (EBSD-based large volume 3D microstructure system [2]) set-up on a recrystallised and sensitised 316L stainless steel sample at a step size of 1 μm. The data set was first re-aligned by rigid methods and then finally by the Smart-align method. The slice images (based on the blue channel of an IPF-X map) were pre-smoothed by a 5 × 5 Gaussian kernel. Four neighbouring slices, two below and two above served as registration references. In a second run this was repeated with 6 neighbouring slices, three above and three below.

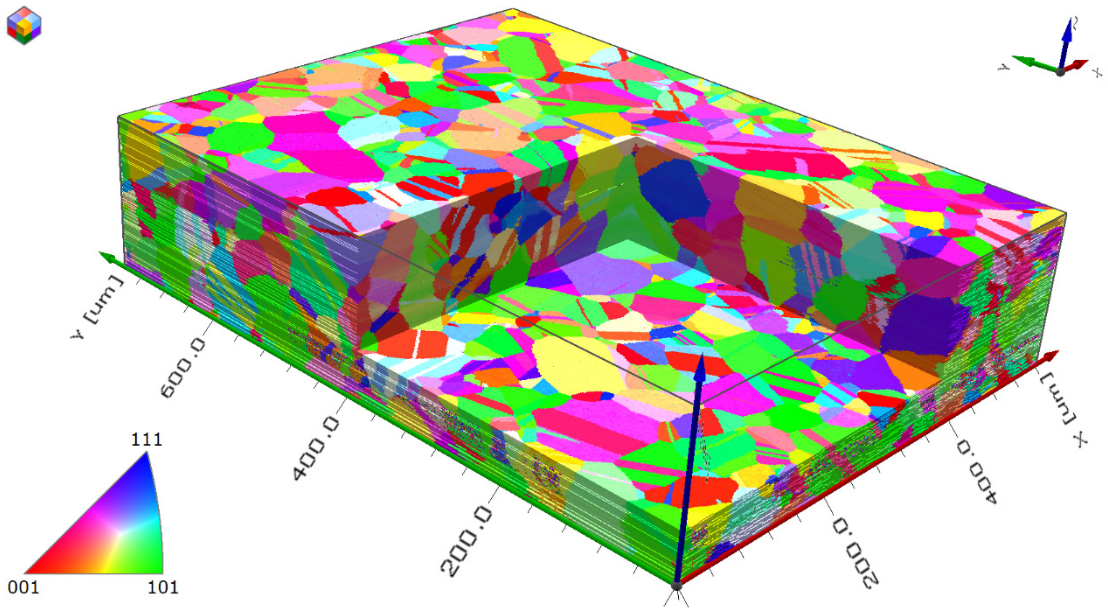

Figure 1. A large 3D orientation data set collected on a recrystallised and sensitised 316L stainless steel sample, comprising 563 ×749 × 167 voxels at a step size of 1 µm, in IPF-x colour code. The data set was rigidly aligned and finally Smart-aligned. Dataset courtesy S. Tsai.

In Fig. 2 the misfit between adjacent slices is shown in terms of the mean interslice low angle grain boundary (LAGB) disorientation angle. This angle is calculated as the mean of all disorientation angles between corresponding voxels in two neighbouring slices. Only voxel pairs whose disorientation is below the low to high angle grain boundary transition angle of 15° are taken into account. As can be seen in Fig. 2, the Smart-align method improves the overall matching between the slices. However, it is also noticeable, that local maxima are less affected by the Smart-align method. A possible explanation is that there the misalignment is still too large to be picked up by the Smart-align.

5. *DESCRIPTION OF INTERFACES IN 3D*

5.1. Boundary descriptions

A key feature of 3D orientation datasets is that they allow to determine the inclinations of internal interfaces, permitting a five-parametric boundary characterisation, including 3 misorientation

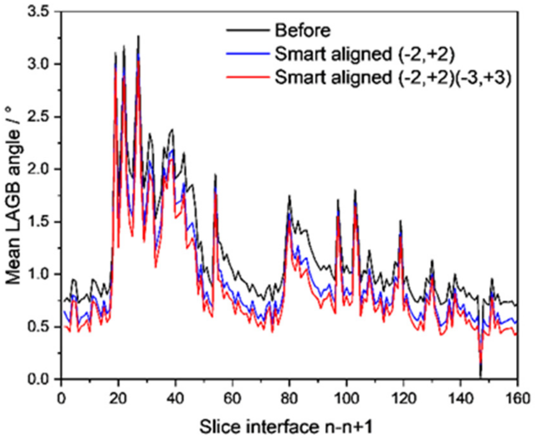

Figure 2. Through thickness evolution of the mean interslice LAGB disorientation angle of the dataset in Fig. 1. Before (black) and after Smart-align (blue) using two neighbouring slices on either side as a reference and a second Smart-align treatment using three neighbouring slices on either side (red).

angles and 2 parameters describing the grain boundary plane. In contrast to 2D datasets, this is possible on a per boundary basis, i.e., in a non-statistical manner. In principle two steps are necessary for the reconstruction of a boundary; a surface must be identified which is then converted into a polygonal mesh of geometric primitives.

Planar boundaries, frequently observed for recrystallisation twins or grains formed during solid state transformations, represent the most straightforward case. For such boundaries, a mathematical plane can be readily approximated to a set of interpolation points, by minimising the sum of the squared perpendicular distances with a total least squares method [29]. Alternatively, a principal component analysis can be applied.

Although a general non-planar boundary can also be mathematically fitted (e.g., as non-uniform rational basis splines or NURBS), a frequent approach for microstructures is to omit the mathematical approximation by directly applying a polygonal mesh to the voxel discrete boundary, see e.g., [30-34]. In essence, this may be achieved through a conversion of the voxel faces that constitute the boundary into mesh triangles. Slightly more interpolating is the so-called Marching Cube (MC) algorithm, originally introduced by [35]. Here, a mesh is generated from a lookup table for a cubic constellation of 8 voxels. However, multi-grain support as well as the topological consistency and correctness of the mesh are easier to realise by splitting the logical constellation into 5 or 6 tetrahedra, as in the Marching Tetrahedra (MT) algorithm [30, 36]. Here a mesh is generated analogue to the MC algorithm for a smaller tetrahedral constellation of 4 voxels, see Fig. 3. The resulting mesh structure consists of boundaries, triple lines and quadruple junctions, any higher order junctions will be decomposed into a combination of first. Compared to the MC algorithm the MT algorithm results in a denser but also computationally more expensive mesh.

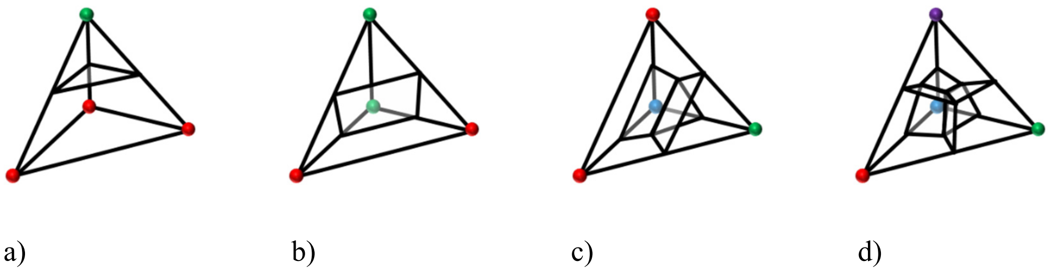

Figure 3. Tetrahedral constellations of 4 voxels belonging to different grains (represented by red, green, blue and purple spheres) [30, 31]. a) 1 boundary with 4 equivalent configurations. b) Similar to a) but only 3 equivalent configurations. c) 1 triple line and 3 boundaries with 6 equivalent configurations. d) 1 quadruple point, 3 triple lines and 6 boundaries with only one possible configuration.

5.2. *Mesh smoothing*

The as-meshed polygonal surface structure still deviates strongly from the physical boundary surface. This is largely due to the voxel discretisation in combination with the meshing algorithm and to a lesser extent still to slice misalignments caused by acquisition errors, as described in sect. 4. This deviation can be efficiently mitigated by a smoothing of the mesh. Materials science literature shows a number of solutions for this, that can be roughly categorised by whether the stage of the smoothing step is either after, see e.g., [30, 32, 34] or before the meshing step, see e.g., [27, 33]. In the following a post-meshing smoothing is outlined, based on [37-39].

A mesh smoothing is achieved by a reduction of the total grain boundary area, very much as during grain growth due to a lowering of a system's Gibbs free energy. Boundaries tend to migrate towards their centre of curvature under the action of a curvature dependent driving force. In consequence, details with a high local curvature are lost first. In the present work this is implemented similar to a vertex grain growth model [38, 39]. For each vertex a total net force is calculated from the vectorial sum of the surface tensions of the adjoining mesh segments as shown in Fig. 4. Boundaries and triple junctions are smoothed alternately to keep their interaction balanced. All quadruple junction positions are kept static.

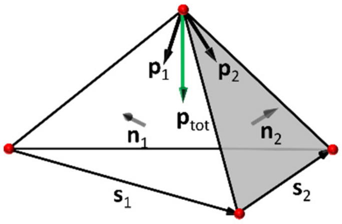

Figure 4. Three mesh triangles, with normals n_i, meet at a common vertex. Here an effective driving force p_{tot} acts as the vectorial sum of the individual driving forces p_i [31, 39].

Any smoothing of the mesh is accompanied by a change in the grain volume distribution. Hence, the vertex motion is constrained in two ways. All vertices at the free specimen surface are constrained within the free surface (except for boundary traces and specimen edges). Furthermore, vertices are also progressively slowed down by a scaling factor the further they deviate from their original positions, according to a user-specified constraint coefficient. The larger the constraint coefficient, the more rapidly the scaling factor will tend to zero.

5.3. Ground truth test

At triple and quadruple junctions, the interaction of multiple boundaries and triple lines leads to a distinctly different smoothing behaviour as compared to within the boundary interior. A suitable ground truth for benchmarking this behaviour can be provided by a 3D Voronoi tessellation where all grains are modelled as convex polyhedrons. This allows it to use planar approximations of the voxel boundaries as a reference for assessing the boundary mesh. This is illustrated by Fig. 5, where a sufficiently sized Voronoi grain is shown in meshed and smoothed condition. The colour coding of Figs. 5a and 5b shows respectively the deviation distance and angle w.r.t. a planar approximation.

In Figs. 5c and 5d the distributions for the same deviations are shown differentiated for the mesh elements at the interior and periphery of the boundaries. Both distributions for the distance as well as the angle are slightly narrower for the boundary interior as compared to the boundary periphery. This is also reflected by Figs. 5a and 5b, where the largest deviations are consistently found at the quadruple and triple junctions. Even though this example depends on a user chosen amount of boundary smoothing and constraining, it may be inferred, that in general crystallographic evaluations of boundary meshes must be interpreted with some caution.

6. APPLICATIONS

Compared to 2D techniques, 3D techniques require much more measurement time for one data set (usually at least several days), thus the necessity of 3D measurements must be considered more critically than in the 2D case and only such measurements should be pursued where 3D information is indispensable. It should be considered that 3D information can often be inferred from 2D measurements or from two mutually perpendicular 2D sections. Such information includes, for example, grain size distribution, grain shapes or volume fraction of phases or microstructure constituents (including pores). Also, the interconnectivity of phases or pores can often, but not always, be inferred from 2D measurements using topological methods [40, 41]. Note also that subsequent slices in a 3D EBSD data set differ only little from each other and therefore do not contribute additional statistical information, in contrast to areas side-by-side that would be investigated in a 2D measurement of similar data size. Truly necessary is 3D information in the following cases.

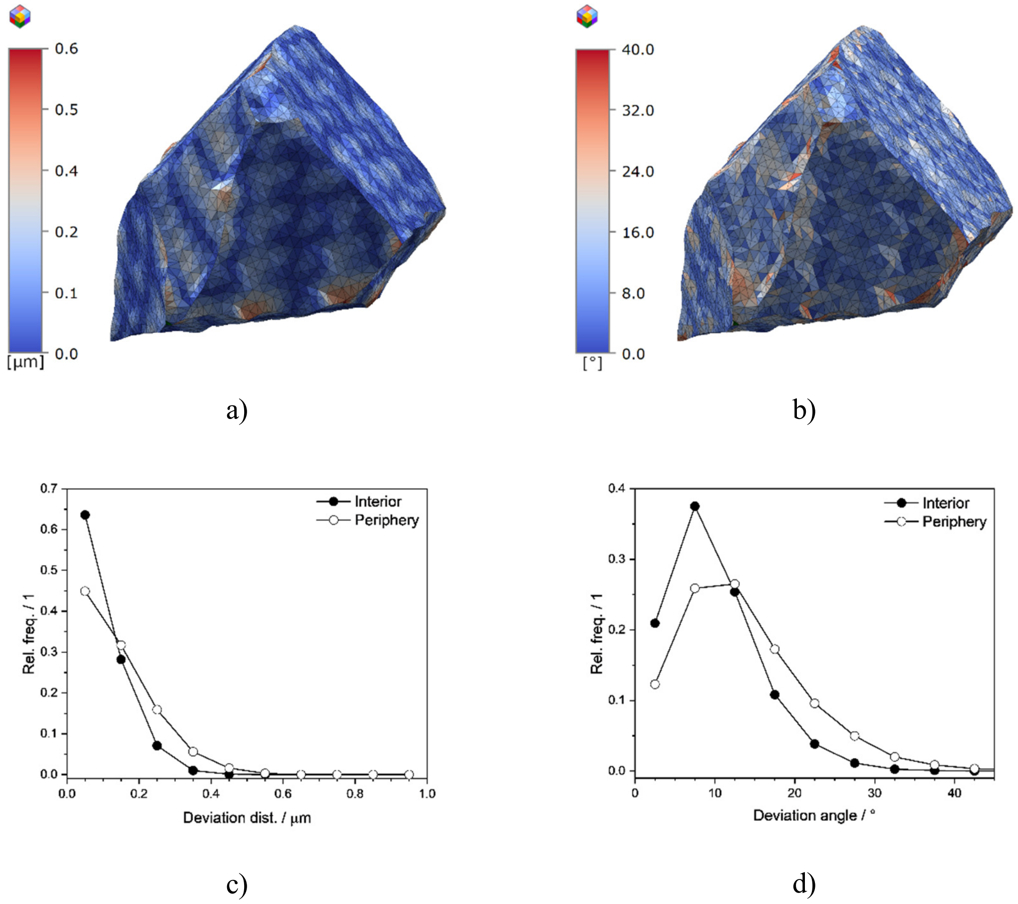

a)

b)

c)

d)

Figure 5. Random Voronoi grain of 2,527 voxels (step size 1 µm) surrounded by 20 hidden neighbours, meshed and smoothed over 100 cycles. The mesh is colour coded by a) deviation distance in [µm], and b) deviation angle in [°] w.r.t a planar fit plane. c) Distribution of the mesh deviation distance in [µm] w.r.t. to a planar fit plane. d) Distribution in [°] of the mesh elements w.r.t. to a planar fit plane. Open symbols indicate peripheral mesh elements adjacent to triple or quadruple junctions, while closed symbols represent interior mesh elements. The deviation distance was determined at the barycentre of each mesh element.

6.1. Morphology and crystallography of inner and outer surfaces

The formation mechanisms of cracks in mechanically monotonically or cyclic loaded materials are of high interest to understand materials damage. Cracks are 3D structures that may or may not follow grain boundaries or specific lattice planes, they may change direction and branch in complex manner. Large volume 3D EBSD is an ideal tool for these investigations [42].

6.2. Morphology and 5-parameter crystallographic character of grain and phase boundaries in conjunction with properties

One of the most important applications of 3D serial sectioning EBSD is the characterisation of grain or phase boundaries (GB or PB) and their properties. In 2D EBSD measurements the crystallography of the GB plane remains unknown, except for special cases where the GB trace may be used to conclude on the GB plane (e.g., for twin boundaries in various materials). A detailed work on the GB character of Σ9 coincidence site lattice (CSL) GBs (double-twin boundaries in fcc materials) [2] showed that Σ9 GBs may have 3 different morphologies and crystallographies, all of which are related to different energies and properties. Low-Σ CSL GBs (Σ = 3, 5, 7, 9) in fcc metals do not have special properties per se, but they have a potential to create low-energy GB planes, which may make them special. Such special behaviour may be, for example, a special resistance to corrosion as it has been investigated on stainless steel. For this the chemo-mechanical polishing serial sectioning approach was used which yields very flat and large surfaces for corrosion test. Figure 6 shows one result with a GB image on the left side and a corrosion image of the same area on the right. Note that in this case only a thin layer of about 15 sections was sufficient to characterise the GBs close to the surface.

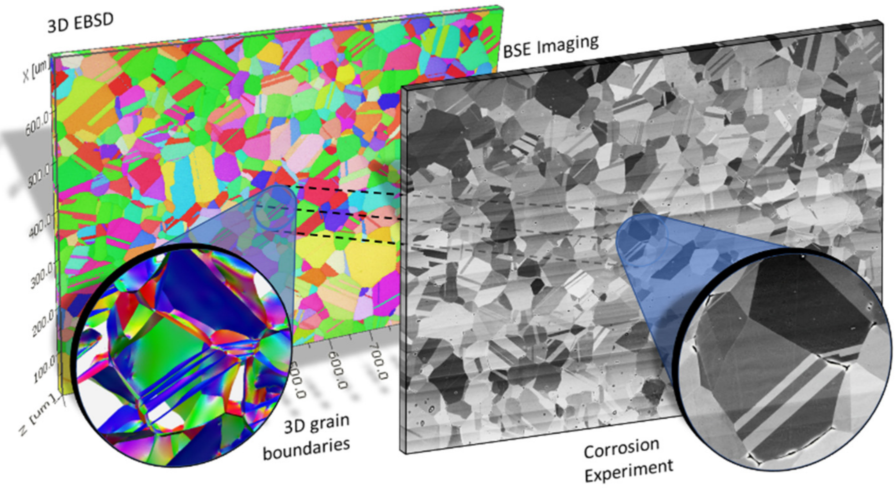

Figure 6. Grain boundary corrosion experiment on a stainless steel. The inset on the left side shows a 3D grain boundary image (difficult to recognise in a 2D image), the right side inset shows details of the grain boundary corrosion behaviour.

Further GB properties that can be correlated with the crystallographic GB character are, e.g., cathodoluminescence in solar cells [43], transport properties, hydrogen embrittlement, or general mechanical strength.

6.3. Crystallographic and morphological nature of nuclei of crystallisation, recrystallisation or phase transformation

Rare features in a microstructure, e.g., nucleation of recrystallising grains in a heavily deformed microstructure are difficult to find and quantify in 2D sections. The true size of a potential nucleus, and its crystallographic environment can only be evaluated from high resolution 3D measurements, e.g., by FIB serial sectioning. Figure 7 shows an example of a growing cube nucleus in a highly cold rolled Fe36%Ni alloy.

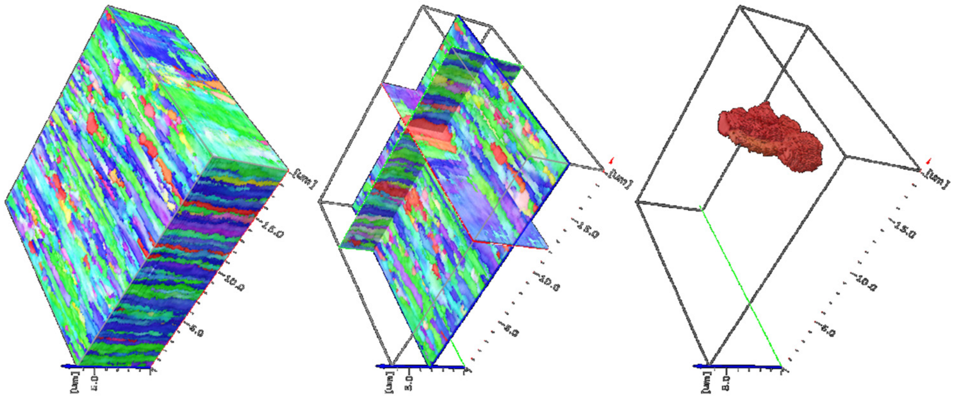

Figure 7. Three different views of a 3D FIB-EBSD map of a rare recrystallisation nucleus in a cold rolled Fe-36%Ni sample (Zaefferer, unpublished data).

Another example which requires the search for and correct description of rare features is, e.g., the characterisation of nucleation points of grains that have been created by rapid solidification during additive manufacturing of materials using laser powder bed fusion.

6.4. *Combination of experimental 3D data with modelling*

As the serial sectioning methods only reflect the status quo of a material, materials processes, like recrystallisation, deformation or phase transformation can only be followed by materials modelling. Furthermore, many modelling tools, like crystal plasticity tools [44] or recrystallisation or grain growth evolution models [45], require detailed 3D input data, which may be delivered by 3D EBSD measurements. Additionally, for all these models dislocation densities play an important role. Geometrically necessary dislocations, GNDs, can be observed and quantified by 3D EBSD techniques [46, 47]. Figure 8 shows an example of a 3D Monte Carlo Potts model simulation, which takes as input a 3D-FIB measured microstructure of a heavily cold rolled FeNi sample. The model uses the stored energy in the dislocations and in the grain boundaries to obtain a proper recrystallisation behaviour of cube-oriented sub-grains.

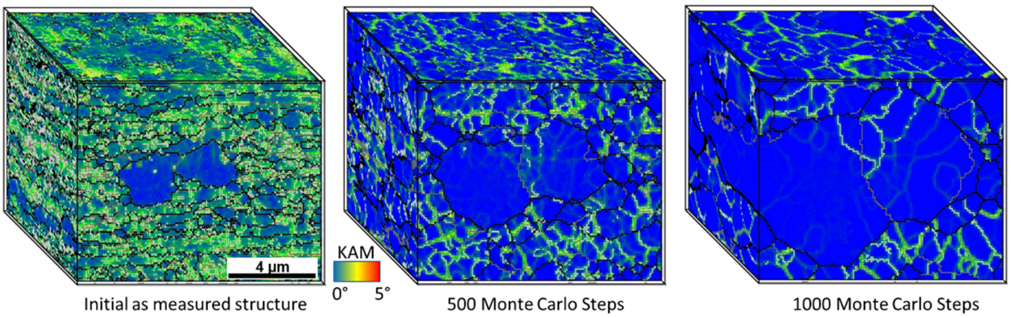

Figure 8. Monte Carlo simulation of nucleation of recrystallisation based on a 3D-FIB measured microstructure of heavily cold rolled Fe 36% Ni. Curvature and dislocation density are taken into account for energy calculation (Zaefferer, unpublished data).

7. CONCLUSIONS

A comparison of tomographic techniques for 3D-EBSD has identified BIB, laser-FIB and chemo-mechanical polishing as promising methods for accurate large volume 3D microstructure characterisation, each with their specific strengths and weaknesses. A correct registration of 3D-orientation data sets remains a central problem in 3D-EBSD, the Smart-align method is a promising solution. The approximation of internal boundaries by polygonal meshes is generally better at the interior of boundaries as compared to the boundary periphery. Alternatively, mathematical approximations appear to be a promising approach. Finally, we identified suitable problems for which 3D-EBSD provides a valuable solution, such as the characterisation of internal interfaces, identification and characterisation of rare features and the support for 3D microstructure modelling.

8. DECLARATION OF COMPETING INTEREST

The authors declare that they have no known competing interests that influence the work reported in this paper.

9. REFERENCES

[1] Schifferer M, Snaidero N, Djannatian M, Kerschensteiner M and Misgeld T 2021 *Front. Neuroanatomy* **15** 732506

[2] Tsai S P, Konijnenberg P J, Gonzalez I, Hartke S, Griffiths T A, Herbig M, Kawano-Miyata K, Taniyama A, Sano N and Zaefferer S 2022 *Rev. Sci. Instrum.* **93** 093707

[3] Rowenhorst D J, Nguyen L, Murphy-Leonard A D and Fonda R W 2020 *Curr. Opin. Solid State Mater. Sci.* **24** 100819

[4] Zaefferer S, Wright S I and Raabe D 2008 *Metallurg. Mater. Trans. A* **39** 374-389

[5] Winiarski B, *et al.* 2025 *IOP Conf. Ser.: Mater. Sci. Eng.* **1324** 012013

[6] Gholinia A, Curd M E, Bousser E, Taylor K, Hosman T, Coyle S, Shearer M H, Hunt J and Withers P J 2020 *Ultramicroscopy* **214** 112989

[7] Winiarski B, Gholinia A, Mingard K, Gee M, Thompson G E and Withers P J 2017 *Ultramicroscopy* **172** 52-64

[8] Echlin M P, Polonsky A T, Lamb J, Geurts R, Randolph S J, Botman A and Pollock T M 2021 *J. Materials* **73** 4258-4269

[9] Watson N J, *et al.* 2022 *Ultrasound tomography*. in: Industrial tomography (2nd Edition). Systems and Applications. [Sawton, U.K.: Woodhead Publishing] 245-273

[10] Jensen D J and Poulsen H F 2012 *Mater. Characterization* **72** 1-7

[11] Yang W, Larson B C, Tischler J Z, Ice G E, Budai J D and Liu W 2004 *Micron* **35** 431-439

[12] Liu H H, Schmidt S, Poulsen H F, Godfrey A, Liu Z Q, Sharon J A and Huang X 2011 *Science* **332** 833-834

[13] Zankel A, Wagner J and Poelt P 2014 *Micron* **62** 66-78

[14] Zhao J, Yu X, Shentu X and Li D 2024 *Cell Tissue Res.* **396** 1-18

[15] Hashimoto T, Thompson G E, Zhou X and Withers P J 2016 *Ultramicroscopy* **163** 6-18

[16] Uchic M, Groeber M, Shah M, Callahan P, Shiveley A, Scott M, Chapman M and Spowart J 2012 *An automated multi-modal serial sectioning system for characterization of grain-scale microstructures in engineering materials* in: Proc. 1st Int. Conf. 3D Materials Science. [Chichester, UK: John Wiley & Sons] 195-202

[17] Guyon J, Gey N, Goran D, Chalal S and Pérez-Willard F 2016 *Ultramicroscopy* **161** 161-167

[18] Groeber M, Haley B, Uchic M and Ghosh S, *et al.* 2004 *AIP Conf. Proc.* **172-1** 1712-1718

[19] Burnett T L, Kelley R, Winiarski B, Contreras L, Daly M, Gholinia A, Burke M G and Withers P J 2016 *Ultramicroscopy* **161** 119-129

[20] Winiarski B, *et al.* 2023 *Laser PFIB for large-volume 3D EBSD: a correlative microscopy perspective.* Thermo Fisher Scientific Inc.

[21] Dong H, Donegan S, Shah M and Chi Y 2023 *Sci. Reports* **13** 21253

[22] Sardhara T, Shkurmanov A, Li Y, Riedel L, Shi S, Cyron C J, Aydin R C and Ritter M 2024 *Nanomanuf. Metrology* **7** 4

[23] Nolze G 2006 *Mater. Sci. Techn.* **22** 1343-1351

[24] Rowenhorst D J, Gupta A, Feng C R and Spanos G 2006 *Scripta Materialia* **55** 11-16

[25] Tong V S and Britton T B 2021 *Ultramicroscopy* **221** 113130

[26] Charpagne M A, Strub F and Pollock T M 2019 *Mater. Characterization* **150** 184-198

[27] Pirgazi H 2015 *Wide field 3D orientation contrast microscopy*. PhD thesis. [Ghent, Belgium: Ghent University]

[28] Jones L, Yang H, Pennycook T J, Marshall M S J, Van Aert S, Browning N D, Castell M R and Nellist P D 2015 *Adv. Struct. Chem. Imaging* **1** 1-16

[29] Moore D and Warren J 1991 *Approximation of dense scattered data using algebraic surfaces.* in: Proc. 24th Ann. Hawaii Int. Conf. System Sciences **1** 681-690

[30] Dillard S, Bingert J, Thoma D and Hamann B 2007 *IEEE Trans. Visualization Comp. Graphics* **13** 1528-1535

[31] Konijnenberg P J, Zaefferer S, Lee S B, Rollett A D, Rohrer G S and Raabe D 2012 *Mater. Sci. Forum* **702** 475-478

[32] Lee S B, Rohrer G S and Rollett A D 2014 *IOP Modell. Simul. Mater. Sci. Eng.* **22** 025017

[33] Rohrer G S, Li J, Lee S, Rollett A D, Groeber M and Uchic M D 2010 *Mater. Sci. Techn.* **26** 661-669

[34] Rowenhorst D, Lewis A and Spanos G 2010 *Acta Materialia* **58** 5511-5519

[35] Lorensen W E and Cline H E 1987 *ACM SIGGRAPH Computer Graphics* **21** 163- 69

[36] Nielson G M and Franke R 1997 *Computing the separating surface for segmented data*. in: Proc. 8th Conf. Visualization '97 [Washington D.C.: IEEE Computer Society Press] 229-233

[37] Brakke K A 1992 *Exp. Mathem.* **1** 141-165

[38] Weygand D, Bréchet Y, Lépinoux J and Gust W 1999 *Philos. Mag. B* **79** 703-716

[39] Barrales-Mora L A 2008 *2D and 3D grain growth modeling and simulation.* PhD thesis. [Göttingen, Germany: Cuvillier Verlag]

[40] Jones A C, Arns C H, Hutmacher D W, Milthorpe B K, Sheppard A P and Knackstedt M A 2009 *Biomaterials* **30** 1440-1451

[41] Hormann K, Baranau V, Hlushkou D, Höltzel A and Tallarek U 2016 *New J. Chem.* **40** 4187-4199

[42] Pirgazi H, Ghodrat S and Kestens L A 2014 *Mater. Characterization* **90** 13-20

[43] Stechmann G, Zaefferer S, Konijnenberg P, Raabe D, Gretener C, Kranz L, Perrenoud J, Buecheler S and Tiwari A N 2016 *Solar Energy Mater. Solar Cells* **151** 66-80

[44] Diehl M, An D, Shanthraj P, Zaefferer S, Roters F and Raabe D 2017 *Phys. Mesomechanics* **20** 311-323

[45] Holm E A, Miodownik M A and Rollett A D 2003 *Acta Materialia* **51** 2701-2716

[46] Kalácska S, Ast J, Ispánovity P D, Michler J and Maeder X 2020 *Acta Materialia* **200** 211-222

[47] Konijnenberg P J, Zaefferer S and Raabe D 2015 *Acta Materialia* **99** 402-414